# AFM interlaboratory comparison for nanodimensional metrology on silicon nanowires

Luigi Ribotta, Alexandra Delvallée, Eleonora Cara, Roberto Bellotti, Andrea Giura, Ivan De Carlo, Matteo Fretto, Walter Knulst, Richard Koops, Bruno Torre, et al.

Measurement Science and Technology



**PAPER** • **OPEN ACCESS**

# AFM interlaboratory comparison for nanodimensional metrology on silicon nanowires

To cite this article: Luigi Ribotta *et al* 2024 *Meas. Sci. Technol.* **35** 105014

OPEN ACCESS
IOP Publishing
Measurement Science and Technology
Meas. Sci. Technol. **35** (2024) 105014 (18pp)
https://doi.org/10.1088/1361-6501/ad5e9f

# AFM interlaboratory comparison for nanodimensional metrology on silicon nanowires

**Luigi Ribotta[1,2,*], Alexandra Delvallée[3,*], Eleonora Cara[2,4], Roberto Bellotti[1], Andrea Giura[1], Ivan De Carlo[4,6], Matteo Fretto[4], Walter Knulst[5], Richard Koops[5], Bruno Torre[4,6], Zineb Saghi[7] and Luca Boarino[4]**

[1] Applied Metrology and Engineering Division, Istituto Nazionale di Ricerca Metrologica (INRiM), Strada delle Cacce 91, 10135 Turin, Italy
[2] PiQuET—Piemonte Quantum Enabling Technology, Istituto Nazionale di Ricerca Metrologica (INRiM), Strada delle Cacce 91, 10135 Turin, Italy
[3] LNE, Laboratoire National de métrologie et d'Essais, 29 avenue Roger Hennequin, 78190 Trappes, France
[4] Advanced Materials and Life Science Metrology Division, Istituto Nazionale di Ricerca Metrologica (INRiM), Strada delle Cacce 91, 10135 Turin, Italy
[5] VSL, National Metrology Institute, Thijsseweg 11, 2629 JA, Delft, The Netherlands
[6] Politecnico di Torino, Corso Duca degli Abruzzi 24, 10129 Turin, Italy
[7] University of Grenoble Alpes, CEA, Leti, F-38000 Grenoble, France

E-mail: l.ribotta@inrim.it and alexandra.delvallee@lne.fr

Received 27 March 2024, revised 3 June 2024
Accepted for publication 3 July 2024
Published 12 July 2024

**Abstract**

Silicon nanowires (NWs) with a cylindrical form are fabricated by means of nanosphere lithography and metal-assisted chemical etching to obtain high aspect ratio nanostructures (diameter of about 100 nm and length of more than 15 μm) on an approximately 1 $cm^2$ area. The nanodimensional characterization of individual NWs is performed by using several techniques, because dimensions at the nanoscale strictly relate to functional performance. In this study, we report the results of an interlaboratory comparison between measurements from a metrological atomic force microscope (AFM) and research AFMs located in different national metrology institutes (NMIs) across Europe and in a university. The purpose of this study is to characterize two measurands: (i) sidewall roughness (*Ra*, *Rq*, *Rz*, *R*sk, *R*ku parameters) extracted from the top profile measured along the nanowire length, and (ii) diameter of the nanowires measured as top-height. To this goal, the nanowires are spread horizontally on a silicon substrate, which has several areas labelled with a pattern of crosses and letters facilitating the measurement of the same NW, in order to study the reproducibility due to different instruments. Measurements show a good agreement between the different NMIs, with a combined standard uncertainty of top-height diameter less than 3%, and with a combined standard uncertainty of roughness parameters well within 5% for *Ra* and *Rq* values.

* Authors to whom any correspondence should be addressed.

Keywords: AFM, roughness, diameter, nanowires (NWs), interlaboratory comparison, uncertainty

## 1. Introduction

For many decades now, numerous scientific reports [1–3] highlight the fact that fossil fuels are limited and harm health and the environment. Renewable sources offer a promising alternative to our global problems and many efforts have been and still need to be realized in order to increase their efficiency. That is why the global Energy Harvesting market size was valued at about USD 3.6 Billion in 2024 and is projected to reach USD 11 Billion in 2031 [4].

Many efforts have been carried out on solar sources in the past decades with, for example, solar photovoltaic global capacity increasing from 6 GW in 2006 to 375 GW in 2023 [5]. Associated technologies evolved from macro- to microscales and are now approaching the nanoscale. With the small size and high surface-to-volume ratio, the promise of nanoscale energy-harvesting devices is increased efficiency with reduced material quantities [6, 7].

In order to achieve these objectives, energy harvesting systems based on nanowires (NWs) are of great interest. NWs are cylindrical nanostructures with diameters ranging from 5 nm to hundreds of nm and aspect ratios from 1 to 100. These nanostructures exhibit useful electrical, electromechanical and thermoelectrical characteristics due to the lateral quantum confinement of electrons and phonons [8–10].

In addition, the realization of porous NWs is relevant for the tuning of thermal transport properties where the pore distribution impacts the thermal conductivity $k$ reducing it to values lower than 2 $W \cdot m^{-1} \cdot K^{-1}$ [11], allowing the future realization of standards for scanning thermal microscopy in the low $k$ range. The presence of pores allows for subsequent modification of the NWs, such as impregnation with organic compounds to obtain organic-inorganic devices interesting for organic electronics or hybrid photovoltaics [12], or to obtain conformal coatings with metallic oxides such as ZnO to tune the functional properties of the NWs ranging from photoluminescence [13] to electrical and thermal transport properties.

However, despite the growing development of NW-type technologies and the numerous potential benefits they offer, the testing and characterization processing pose ongoing challenges. For example, it is still difficult to make the link between measurements carried out at the nanoscale and results on a larger (micrometric) scale. Nanometrology plays a crucial role in ensuring the traceability and reliability of measurements through the development of methods specifically tailored to instrumentation at the nanoscale. One of the aims of the studies realized in the NWs project (19ENG05 NWs, EMPIR programme [14]) is to respond to the lack of methodologies for the NWs characterization while developments are already well advanced for roughness measurement by atomic force microscopy (AFM) for critical dimension for example [15, 16]. The aim of this particular study is to target the roughness and dimensional characterization at the nanoscale.

Indeed, many articles report on the effects of roughness on the performance of electronic devices (*e.g.* transistors, solar cells), particularly their impact on physical properties such as electrical [17, 18], optical [19], electrochemical [20], thermal, electron and phonon transport [10, 21–23].

Previous work on crystalline Si NWs with similar diameters has showed that phonons are strongly scattered by the wire surface, revealing a strong dependence of the conductivity on the diameter of the wire [23]. At a high surface roughness, the thermal conductivity can even be reduced by two orders of magnitude compared to bulk Si [24, 25].

In this work, we report an inter laboratory comparison study on AFM dimensional and surface roughness characterization on silicon NWs, involving different national metrology institutes in Europe. The proposed methodology connects established methodologies for quantifying nanoparticles with standardized approaches for nanoscale step heights. The characterization of nanomaterials is a critical step in the development of technologies where these are implied. In this framework, developing and establishing standardized measurements protocols through inter laboratory comparisons is required for single types of nanomaterials and targeting the measurands relevant to various applications. Such well-developed characterization method can be implemented in a hybrid characterization approach [26–29]. The use of multiple, well-assessed, characterization methods is a growing and essential practice for a broader comprehension of nanomaterials structural, physico-chemical and functional properties. Next to providing the roughness properties of the wires, with their uncertainties evaluation, the results of this study will also help demonstrate the comparability of the measurement results obtained with various instruments.

## 2. Fabrication of nanowires and deposition on a patterned substrate

The realization of porous Si (pSi) NWs relies on three main steps: polystyrene nanosphere (PS NS) lithography, gold thin film deposition via evaporation, and metal-assisted chemical etching (MACE) [30]. Initially, a commercially available Si n+ doped substrate (MEMC Electronic Materials), with a resistivity of (27–47) mΩ·cm, was cut into squares with sides of 1.5 cm. These samples were then cleaned in an ultrasonic bath containing acetone and subsequently isopropanol, followed by drying under nitrogen flow. The samples surface was made hydrophilic employing an oxygen plasma (Bdiscom Plasma Matrix) at 40 W for 6 min. $O_2$ plasma was chosen over the piranha solution due its reduced safety risk and being less time consuming. Afterward, the substrates were patterned through

polystyrene (PS) nanospheres (NS) lithography, which consists of the drop-casting and spin coating of 60 µL of aqueous solution, with 194 nm diameter commercial PS NSs (PS02008 BANGS Lab). The coating part was carried out using a programmable spin coater (Laurell Technologies), employing a two-step program with selected spinning speed ($\omega$) and acceleration ($\alpha$). The two steps were set to last for 10 and 30 s in sequence, with $\omega$ and $\alpha$ 500 rpm and 410 rpm·s$^{-1}$ respectively for the first part and 2500 rpm and 820 rpm $\cdot$ s$^{-1}$ for the second part. These parameters were optimized to achieve a monolayer of PS NSs with a hexagonal closed packed structure, minimizing defects and maximizing the size of the grains (see figures 1(a) and (b)) [11, 31]. Afterward, the samples were treated with argon plasma etching with 75 W RF power at a pressure of about $10^{-2}$ mbar. This process aimed to reduce the diameter of the PS NSs without compromising their circular shape, passing from the initial diameter of 194 nm to the final one of 100 nm (see figures 1(c) and (d)). The reduced NSs pattern was then used as a shadow mask for 20 nm of gold deposition, using e-beam evaporation. An ultrasonic ethanol bath was employed to perform the NSs lift-off, to obtain a pattern of circular voids on the gold layer, which constitutes a mask necessary to carry out the porous silicon NWs etching (see figures 1(e) and (f)). The final step in the realization of pSi NWs involved MACE. This process is able to selectively etch silicon, due to the presence of a metal catalyst, in this case, the antidot mask of Au. The etching solution used consisted of HF (50%): $H_2O_2$ (35%): EtOH in a ratio of 10:1:3. In this solution, $H_2O_2$ induces the oxidation of silicon by reducing at the Au surface and injecting holes at the Au/Si interface. HF then dissolves the resulting silicon oxide, below the Au antidot mask, leading to the definition of an array of silicon NWs with porous structure when the original substrate is highly doped, as in this case. [30, 32]. The samples were soaked in the etching solution for 50 min, a time sufficient to obtain NWs longer than 15 µm, then the process was stopped by rinsing the samples with ethanol and finally left to dry in air (see figures 1(g) and (h)). MACE is a competitive technique respect to Deep Reactive Ion Etching, able to produce very high aspect ratio (over 1:150 in this case). The need of such long NWs is connected to the thermal conductivity measurements, in which the NWs are hung onto MEMS platforms with suspended beams of micrometric scale.

A scanning electron microscope (SEM) characterization (FEI Inspect F available at the Nanofacility Piemonte at INRiM QR Micro&Nanolaboratories) was carried out after each fabrication step, at 10 and 30 kV and a working distance of 10 mm, in order to evaluate the quality of the processes carried out and to tune and optimize the fabrication parameters.

The NWs obtained with this electroless etching method can have a porosity content depending on the initial doping level of the substrate and time of etching. However, the porosity cannot be measured by AFM, which only targets surface roughness. The NWs were dispersed on a TEM grid and the image was acquired by high-angle annular dark-field scanning transmission electron microscopy using a Thermo Fisher Scientific Tecnai Osiris S/TEM, operating at 200 kV and equipped with a high brightness electron source. Figure 1(k) reports a scanning transmission electron microscopy (STEM) image of a single nanowire showing its porosity and surface roughness.

Such porosity has critical dimensions lower than the curvature radius of the AFM tip used for the subsequent characterization, hence cannot be fully resolved. However, some asperities are visible on the nanowire surface, these may be originated during the etching process or may be due to fragments of other NWs electrostatically attached to the NW of interest. Such surface modifications are detected as imperfections and surface roughness through AFM analysis.

In this study, NWs were then transferred onto three (9 × 9) mm patterned silicon substrates (figures 1(i), (j) and 2), designed by LNE and fabricated by C2N (Centre for Nanoscience and Nanotechnology) CNRS, Palaiseau, France) [28], in order to be able to locate easily the same set of NWs with different instruments. Letters and crosses were lithographed on these substrates. A 9 × 9 mm grating of areas are marked with numbers. 16 × 16 crosses, 15 µm apart from each other, are etched in each numbered zone (figure 2). Each substrate is also referenced. A previous study had evaluated the roughness of this substrate to be equal to 0.3 nm ($S_q$) [28]. It was also confirmed by the measurements made by the partners. The transfer of the NWs occurs using a laboratory paper tissue that collects the NWs from their matrix through electrostatic forces. These are then released randomly on the marked silicon chip. The success of the NWs transfer can be checked through optical microscopy and can be repeated if necessary. The random release of NWs can result in the presence of isolated NWs laying horizontally on the marked sample, which can be characterized by AFM, and in the presence of agglomerates of NWs. The agglomerates cannot be analysed by AFM without compromising the tip, for this reason the NWs transfer is previously characterized by optical and scanning electron microscopy to highlight the suitable region for the AFM analysis. In figure 2, the green regions indicate the presence of isolated NWs while the red regions indicate the presence of bundles and they are not approached with the AFM tip.

## 3. AFM instruments involved in the intercomparison

### 3.1. INRiM metrological AFM

The samples are analyzed with the INRiM metrological AFM [33] in order to give a reference measurement.

INRiM metrological atomic force microscope (mAFM) is a customized instrument with an AFM head placed on a sample-moving mechanical structure. Tip-sample movements while scanning the sample are monitored by interferometers, ensuring a direct traceability to the SI.

Instrument traceability is achieved through in-situ interferometric calibration of the vertical scanning device ($Z$-axis) and interferometric measurement (metrological closed loop control) of lateral displacements ($X$- and $Y$-axes) during relative tip/sample movement. The wavelength of the He–Ne heterodyne laser Zeeman modulation type source of the interferometer (633 nm) is calibrated with respect to the Mise en Pratique (MeP) [34] sample length laser He–Ne every 5 years.

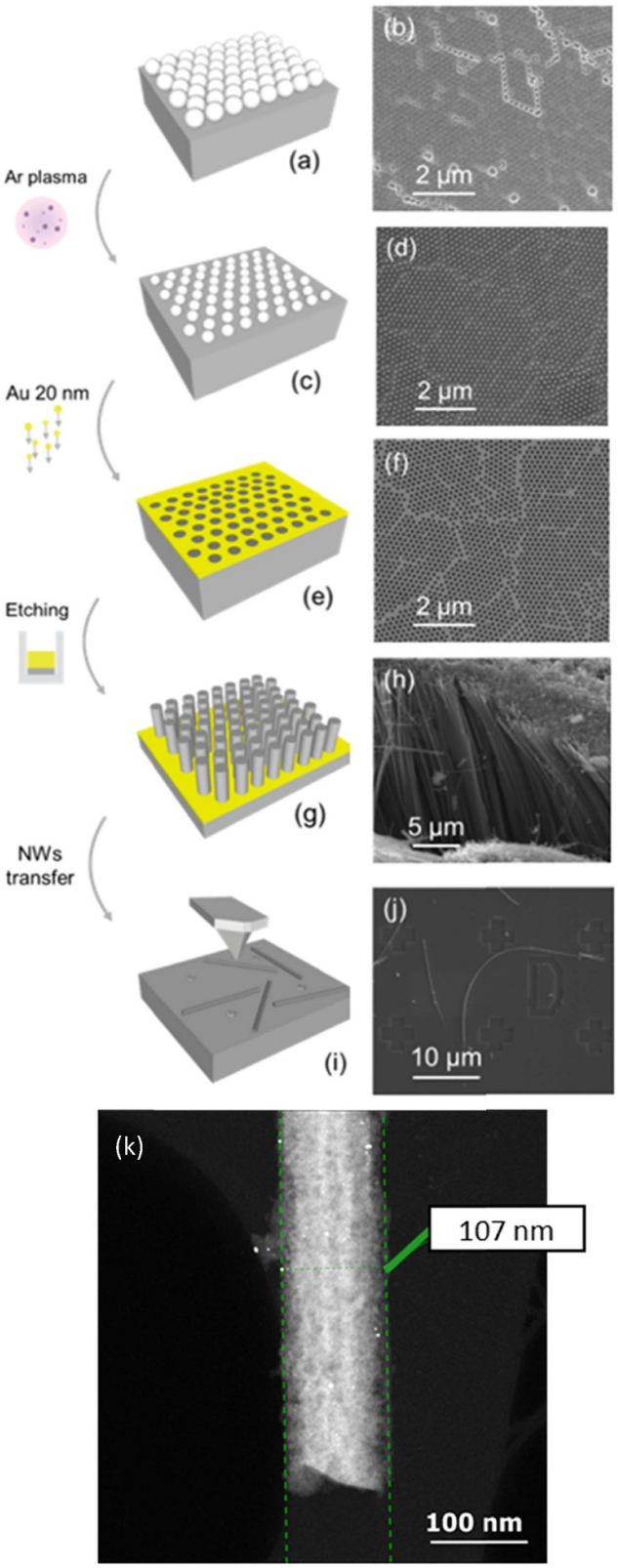


**Figure 1.** Schematic representation of the pSi NWs fabrication. Each fabrication step is illustrated with both the sketch and the SEM image. (a), (b) Deposition of polystyrene nanospheres NSs (diameter 194 nm) on the silicon wafer by spin coating at different rotational speeds. (c), (d) Reduction of NSs diameter to 100 nm by argon plasma. (e), (f) Deposition of 20 nm of Au and lift-off of the NSs to obtain the pattern of circular voids on the gold layer. (g), (h) Metal-assisted chemical etching to obtain the porous silicon nanowires with very high aspect ratio (NW length $>$ 15 µm, diameter 100 nm, aspect ratio 1:150), is unachievable by dry etching methods. (i), (j) Transfer of the nanowires NWs on a solid silicon substrate with markers, where they lay horizontally, and their sidewalls can be probed by AFM. (k) STEM image of a single nanowire, where the roughness can be appreciated.

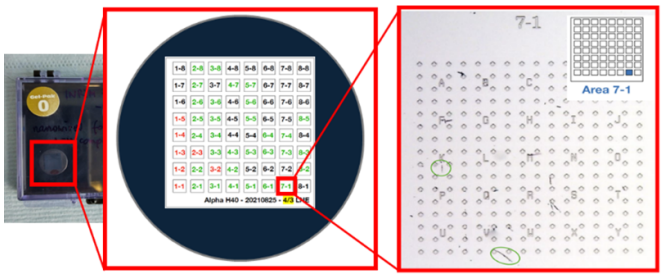


**Figure 2.** (left) Photography of one of the three samples used for the study. (center) Schematic view of the different numbered zone on a substrate. (right) Optical microscope view of a numbered zones (here zone 7–1) on a marked silicon substrate (9 mm × 9 mm) where are deposited nanowires. Distance between two crosses is 15 µm.

The mAFM is located in the length and mass laboratory at INRiM, located 9 meters underground to reduce the impact of environmental vibrations from city traffic, with controlled temperature and relative humidity, set to $T = (20.0 \pm 0.1)$ °C and RH $\sim (50 \pm 15)$% respectively, according to ISO 1 [35].

The AFM measurement modality used is non-contact with amplitude modulation. Measurements are performed using commercial $n$-type silicon tips by $\mu$Masch, with a nominal radius of 8 nm, a nominal resonance frequency of 325 kHz (frequency range 265–410 Hz) and a nominal force constant of 50 N·m$^{-1}$ (force constant range 20–80 N·m$^{-1}$).

Images with dimensions of about 6 µm × 6 µm were taken with resolution of (1024 × 1024) pixels.

### 3.2. AFM in PiQuET cleanroom

The AFM Park Systems NX20 is an instrument devoted to measure large sample, up to the dimensions of a six-inch wafer.

The AFM Park Systems is installed in a cleanroom laboratory with ISO 6 particle control [35] and controlled temperature set to (20 ± 0.5) °C and a relative humidity of (50 ± 10)%.

The AFM measurement modality used is non-contact with amplitude modulation. Measurements are performed using commercial $n$-type silicon tips by Nanosensors, with a nominal radius of 8 nm, a nominal resonance frequency of 330 kHz (frequency range 204–497 Hz) and a nominal force constant of 42 N·m$^{-1}$ (force constant range 10–130 N·m$^{-1}$).

Instrument traceability is achieved through the calibration by using step-height transfer standards TGZ02 provided by MikroMasch (nominal height: 100 nm), previously calibrated by INRiM metrological AFM with 1.1 nm uncertainty ($k = 1$) relative to the height measurement.

### 3.3. LNE AFM

The AFM images have been acquired with a Veeco Dimension with a Nanoman $V$ controller. This AFM is available on LNE's CARMEN (Metrological Characterization of Nanomaterials) platform. The laboratory is controlled in temperature, pressure and humidity and well characterized in terms of noise, drift, and other sources that can enlarge the measurement uncertainty [36]. The temperature achieved in the enclosure reach 32 °C as the electronic part are inside. The instrument is placed on a massive concrete block in order to avoid vibration issues and in an acoustic enclosure. All the images realized on the NWs were acquired with OTESPA-R3 tip (nominally 7 nm tip radius, Bruker' specification) in intermittent contact/tapping mode. It operates in close-loop control.

The calibration had been realized before and after the NWs measurement step, with a calibration grid P900H60 [28]. The calibration grating has an indicative pitch of 900 nm and a height of 60 nm. The calibration of this grating was realized with the LNE's metrological AFM [37] with 0.5 nm uncertainty ($k = 1$) relative to the height measurement.

### 3.4. VSL AFM

At VSL the Veeco Dimension 3100 was used for this investigation. Due to the fact that the measuring range was larger than 100 nm, the instrument was calibrated in the $Z$-axis with step height standards leading to and not using virtual standards [38]. The calibration of the lateral scales was considered of minor importance since the required measurands only depend on the $Z$-values, so nominal calibration coefficients were used for the lateral scale. All measurements were performed in tapping mode with probes of type NuNano SCOUT 350 H HAR with a nominal tip radius of 5 nm.

### 3.5. PoliTo AFM

The AFM used is an MFP-3D Bio model from Oxford Instruments Asylum research coupled with an inverted Optical microscope (Nikon Ti–S) allowing for the contextual optical and scanning probe investigation of the specimen.

The microscope is specifically designed to prevent crosstalk by separating the vertical nano-positioning system ($z$-channel), integrated in the microscope head, and horizontal movements ($x$-and $y$-channels) physically located on a separate scanner. The three channels are driven by piezoelectric actuators embedded in electro-eroded stainless-steel frames to allow maximum linearity on the movement, hosting an LVDT positioning sensor for the detection and correction of the piezo position on $x$-, $y$-, and $z$- channels. Scanner capabilities are 15 µm $Z$-range with $Z$ sensor noise $< 0.25$ nm, $x$-$y$-channel range 90 µm with sensor noise $< 0.6$ nm, DC height noise $< 50$ pm.

Additionally, the setup is installed in an acoustic hood ATCBCH ensuring an acoustic insulation $> 30$ dB and a temperature stabilization better than 0.1 °C, and includes an active vibration insulation platform (Halcyonics Micro 40) effective at starting frequencies of 0.6 Hz and with guaranteed isolation performances of 25 dB at frequencies $> 5$ Hz 25 and 40 dB for vibration frequencies $> 10$ Hz.

Measurements were performed in intermittent contact AC Mode by using tips from Asylum AC 160 TSA (res Freq 380k Hz, spring constant 62 N · m$^{-1}$, with nominal radius 7 nm. Laboratory conditions were $T = 25$ °C and RH (35–45)%.

Instrument traceability is achieved through the calibration of TGZ02 step-height standard against INRiM metrological

AFM. In fact, the same standard, same operator, same procedure was used to calibrate both PiQuET and PoliTo AFMs, so the calibration of the two instruments are comparable.

## 4. Measurands

Since at the nanoscale dimensions strictly relates to functional performances, the measurands we decided to study are the diameter of the NWs and the roughness along the wire.

### *4.1. Diameter*

The diameter of the circle base of a nanowire can be extracted with the same approach used for measuring the diameter of spherical nanoparticles (NP) [36, 39, 40].

As reported in the American ASTM E2859-11 [41] and the NPL GPG 119 guides [42] and Vobornik *et al* [43] a method that can be used to measure the diameter of isolated spherical NPs dispersed onto a flat substrate is the extraction of the top-height. More in detail, once the cross-section profile of the NPs is extracted (figure 3), the average substrate baseline is subtracted from the peak height to find the NP top-height.

But unlike spherical NPs, the diameter of a nanowire cannot be extracted from a single top height point as the height/diameter of the nanowire can vary along its entire length. Indeed, along the total length diameter variation of few nanometres can occur due to the continuous immersion in the etching solution during the fabrication. Because of this, the top-height point had to be extracted on several profiles along the nanowire, ideally on each line of the nanowire AFM image. As a result, a profile all along the nanowire can be determined and can also be used to determine the roughness parameters all along the NWs (section 4.2).

Furthermore, in sample preparation some NWs can randomly join together creating a thicker rod that changes its height (Paragraph 2 and figure 3(b)). It can therefore happen that NWs do not touch the substrate all along the wire.

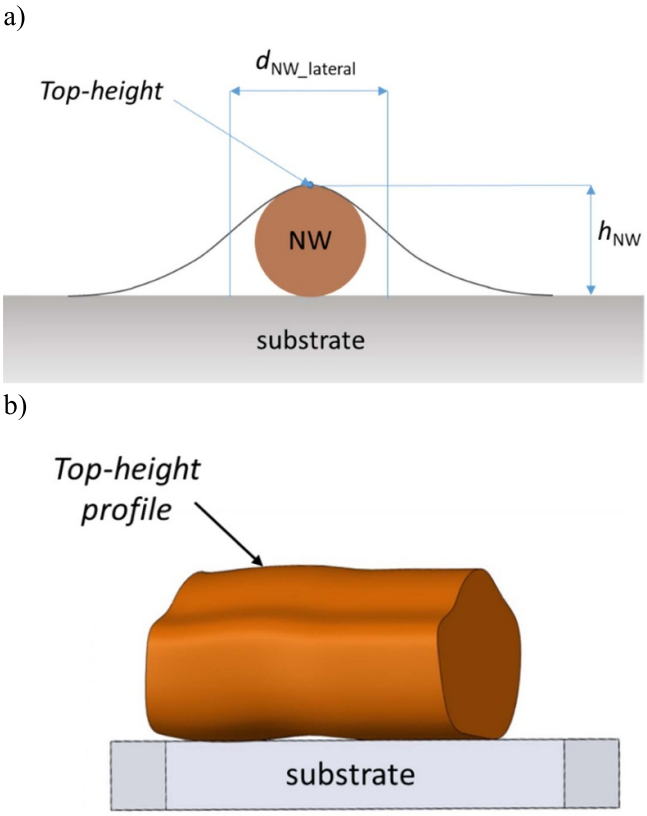


**Figure 3.** (a) Cross section of a nanowire deposited onto a surface. The grey line is a profile achieved by the tip: the lateral diameter ($d_{NW\_lateral}$) is enlarged by a convolution between the tip and the nanowires. The diameter can be extracted from the height of the NW $h_{NW}$. The height of the nanowire is defined as the vertical distance between the point called 'top height' and the substrate. (b) 3D sketch of a nanowire.

### *4.2. Roughness parameters*

Surface characterization regards the analysis of the roughness of the profiles, according to the ISO 21920:2021 [44]. Please note that ISO 21920-2:2021 transposes and replaces ISO 4287:1997, ISO 13565-2:1996, ISO 13565-3:1998.

The roughness amplitude parameters characterize the surface based on the *Z*-axis deviations of the roughness profile from the average line [33, 45]. In this study, the different partners extract along the NWs length the following parameters: *Ra* (average roughness), *Rq* (root-mean-square roughness), *Rz* (maximum height of the roughness profile), *R*sk (roughness skewness), and *R*ku (roughness kurtosis) [45].

## 5. Development of a protocol for nanodimensional measurements with AFM on NWs

At first, the deposited NWs to be considered in the study had to be selected. Indeed, during the deposition, it happens that they form clusters and large bundles, so not all regions are suitable for the AFM measurements, because bundles can cause breakage and wear of the tip. Preliminary observations were carried out over large area on the patterned substrate by means of optical microscopy. A scheme of the silicon chip is given in figure 2 with different areas marked with numbers, letters and crosses. The green areas present isolated NWs suitable for AFM measurements, while the red areas present NWs agglomerates and were disregarded.

Only regions featuring sparse NWs are imaged by SEM, as in figure 4, in order to provide information before AFM measurement sessions.

After the preliminary observations, the patterned silicon chips with NWs spread horizontally were circulated among the institutes, and at least 10 NWs per each sample were analyzed for a reliable statistical data evaluation.

For AFM images acquisition, the participants respected a protocol specifically designed for this interlaboratory comparison. Tapping mode is recommended [46], the image must have (1024 × 1024) pixels with a scan size of (6–10) µm, an imaging force in the range 5–15 nN and a scan speed of about 0.4 Hz. All the AFM must be calibrated. Moreover, the participant were asked to wait few hours to reach the thermalization

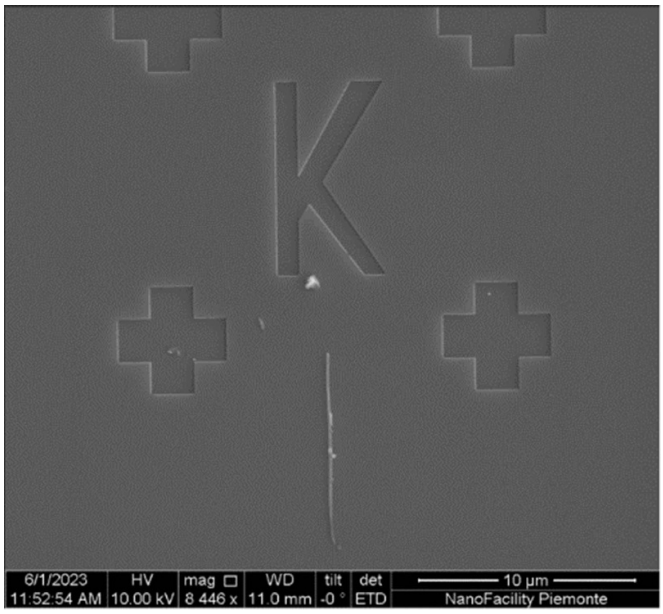


**Figure 4.** SEM image of an area with NW deposited on marked silicon substrate. Zone linked to the selected green area of .figure 2

of the instrument in there enclosure before realizing the measurement. In fact, many drift (*X,Y,Z*) could be observed due to this phenomena as it was pointed out by Marinello *et al* [47].

It has to be noted that all participants measure the same NWs, thanks to the patterned substrate that helps the localization onto the sample.

In order to extract the roughness parameters from the raw measurement data, it was found that a simple plane correction was not sufficient because of residual distortions from tip instabilities and 1/f noise (figure 5). Correction of these distortions was performed by isolating the data points representing the substrate only, and then correcting each scan line for tilt and offset of the substrate line by line (figure 6). In order to eliminate measurement distorsions by tip effects and 1/f noise, the individual measurement fields were first leveled by manually selecting three points representing the background plane. After subtraction of this plane, a mask is constructed with those data points that represent the background. The selection of points that represent the background is based on the distance to the median value (threshold masking). The selection is implemented as a cumulative process for an ever decreasing margin around the updated median value until the mask is stable. Finally the mask is used to perform first order corrections of the individual image lines.

Qualitative inspection of the result of this correction was performed by visual inspection of the substrate image and qualitatively by the resulting histogram representing the substrate data. A very sharp histogram for the substrate data corresponds to optimal alignment of the scan lines (figure 7) and a reduction of the width of the peak corresponding to the substrate. The alignment of this peak with 0 nm is the result of the line-by-line correction.

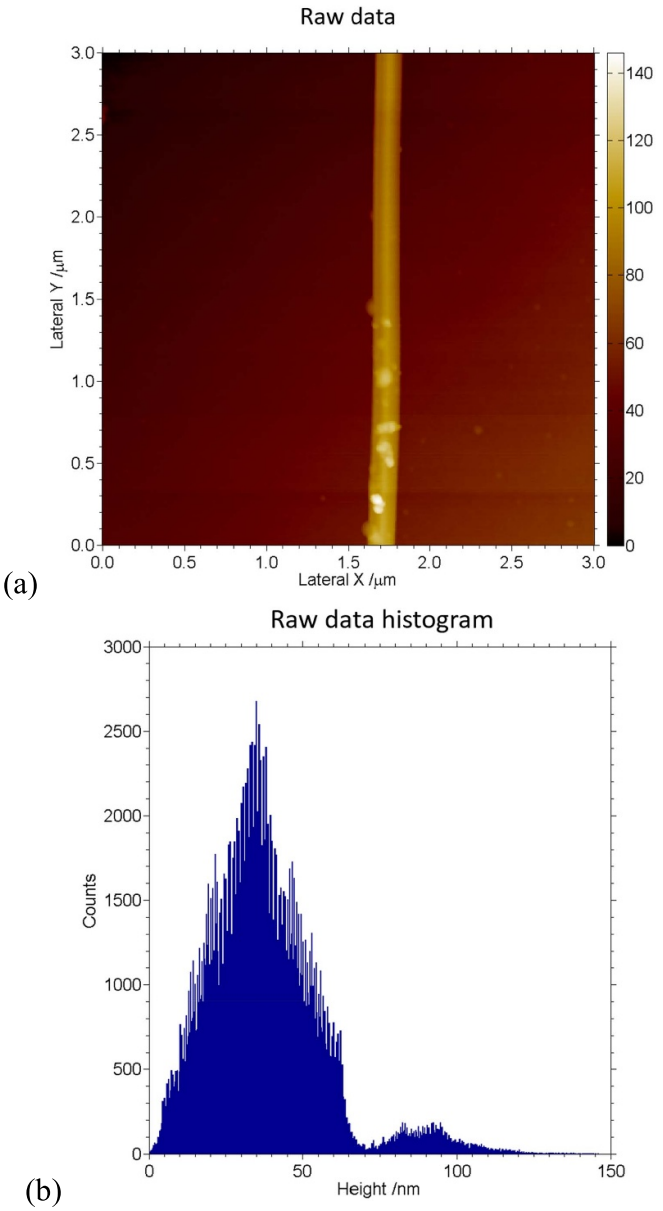


**Figure 5.** (a) Raw AFM data usually present a tilt due to misalignment between the tip scan plane and the sample plane, as becomes clear when the data is represented as a histogram (b).

Then the participant were asked to extract the diameter from the top-height (paragraph 4.1) in zones free from contamination. In order to achieve this point, cross-sections were drawn from the previously levelled images all along the NW. A mean profile was calculated from those ones, and the top-height of this mean profile was determined to give a value for the diameter.

Finally, each pixel representing the top-height along the NW length was extracted to draw a 'top-height profile' (figures 8 and 3(b)).

The roughness parameters are calculated from this one after removing a Gaussian *L*-filter with $\lambda = 2.5$ µm (figure 9) [44].

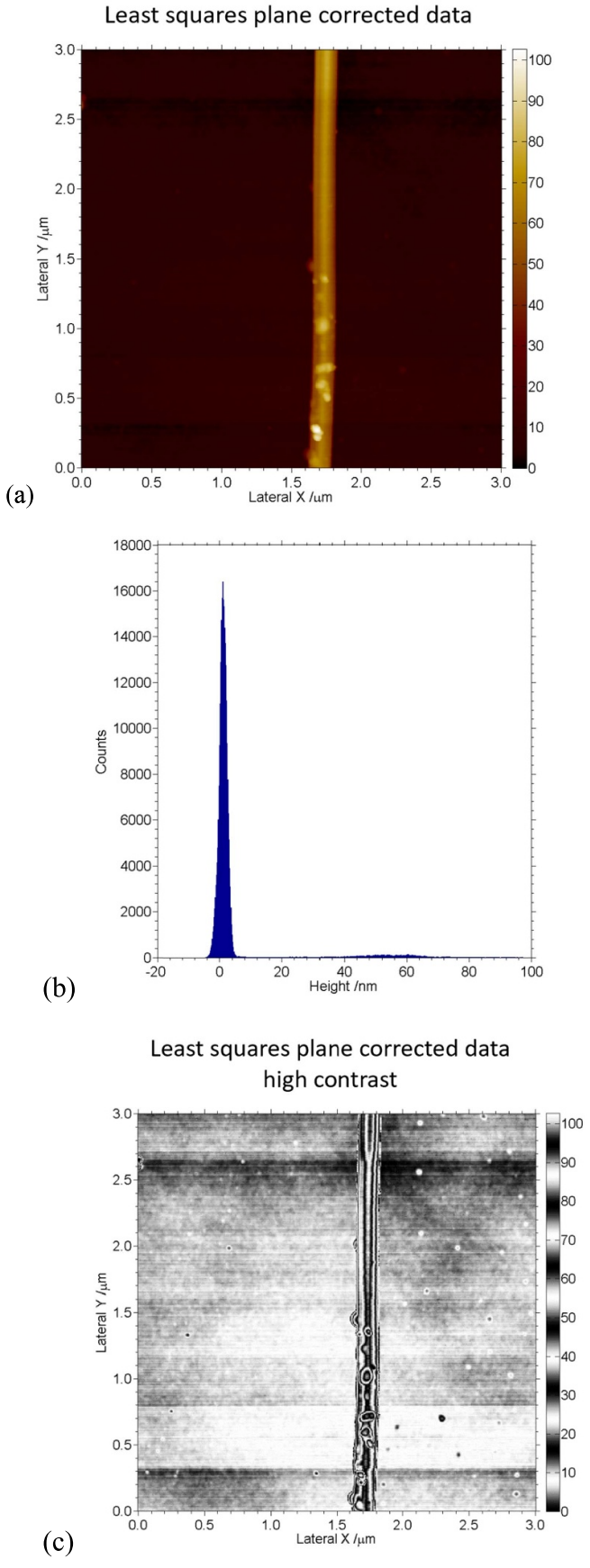


**Figure 6.** By subtracting the least squared plane (a), the background apparently becomes levelled as demonstrated by the sharp peak at zero in the histogram (b), but a high contrast colormap (c) reveals tip changes and 1/f noise.

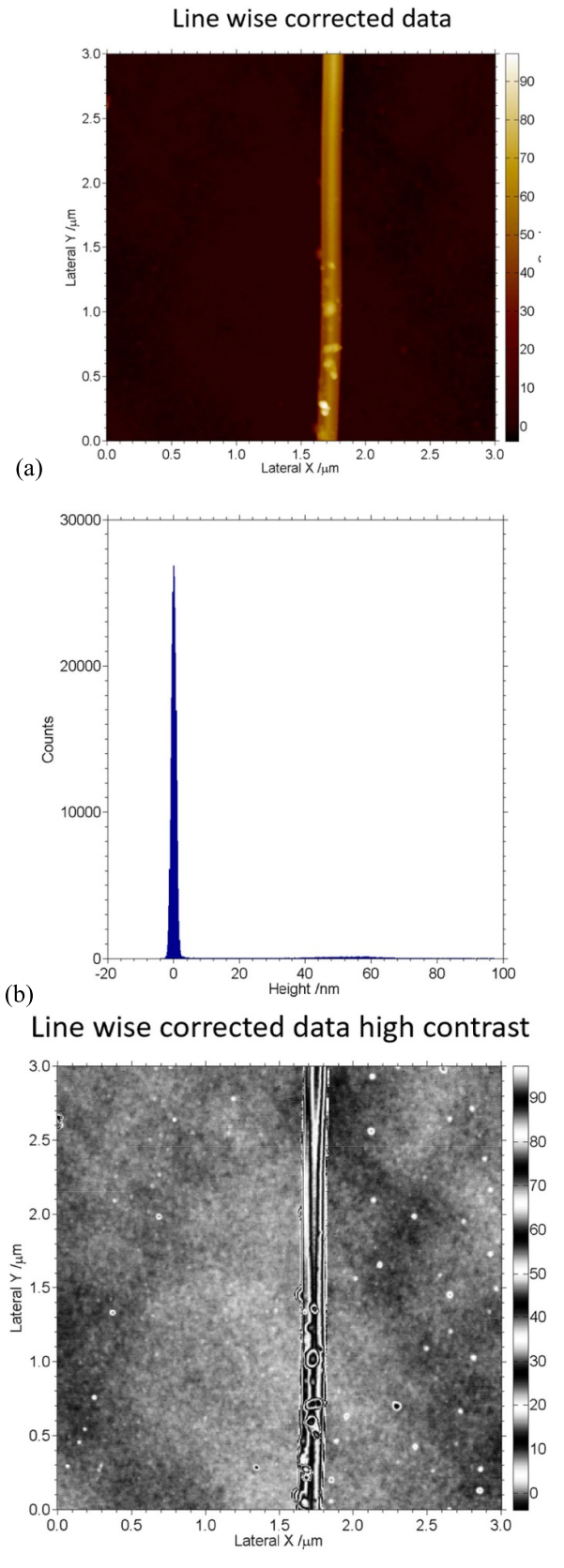


**Figure 7.** To minimize the effects of tip changes and 1/f noise, line wise correction of the levelled data is required. Although the visual appearance of the corrected field (a) is the same as the least squares corrected field, the histogram (b) now shows the highest possible histogram peak and the high contrast map (c) shows no remaining distortions.

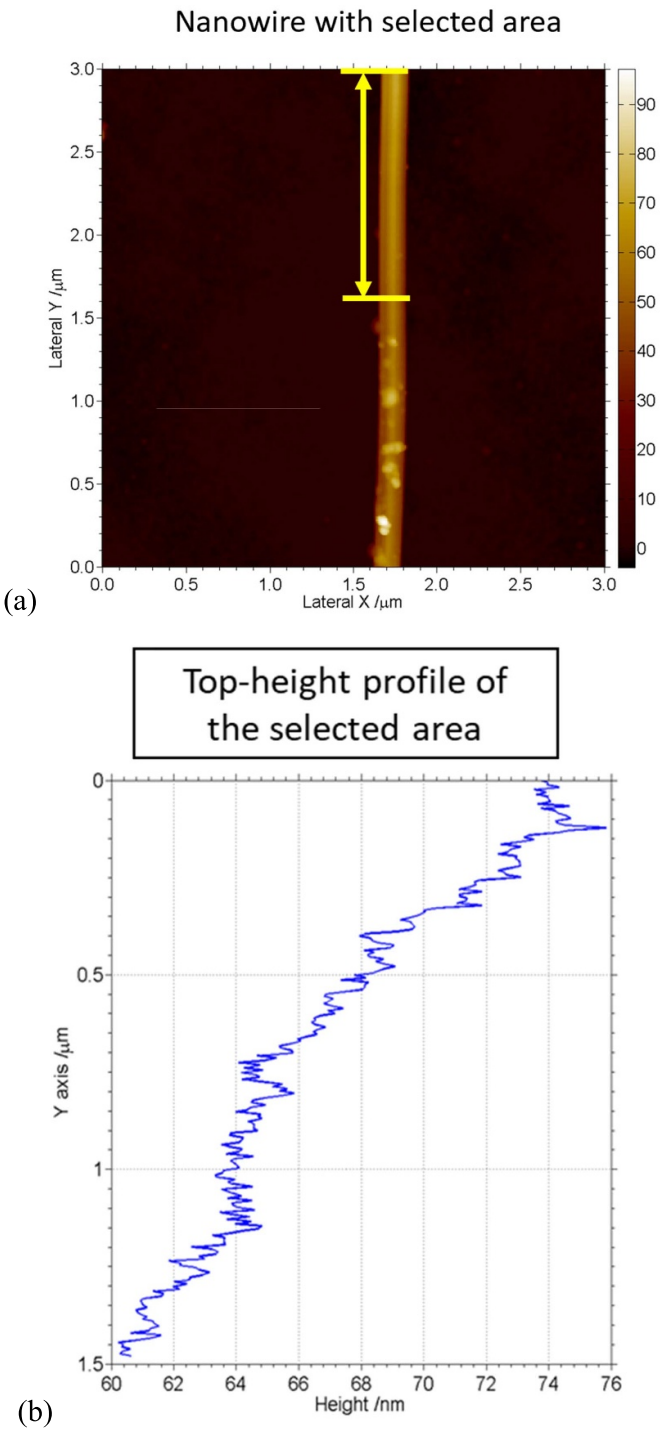


**Figure 8.** The analysis of the nanowire surface is based on the selection of areas where there is no obvious contamination. The yellow arrow (a) shows the region for which the 'top height' profile was extracted, as shown in the (b) 'top height profile' along the wire.

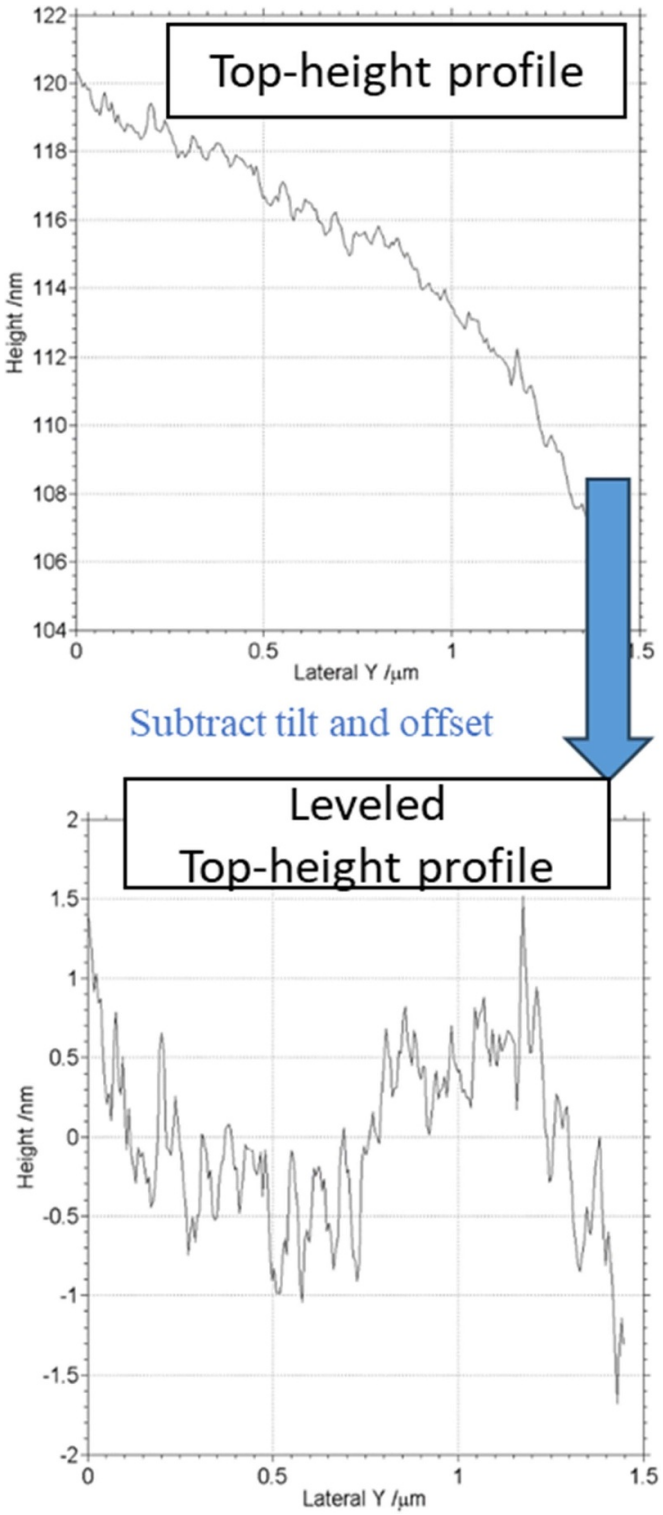


**Figure 9.** The leveled top-height profile was determined by first subtracting the tilt and offset from the raw top height profile, and filter by means of a 2.5 μm high pass cut-off filter.

## 6. Results and discussion

### *6.1. Independent results from partners*

In this section, the results regarding the top-height diameters and roughness parameters extracted by the analysis of the three samples are reported.

In order to keep the results anonymous, the five partners in paragraphs 6 and 7 are named as *A, B, C, D* and *E*. The five participants are detailed in section 3.1 to 3.5.

Figure 10(a) reports the mean weighted value of diameters with the standard deviation and is consistent with

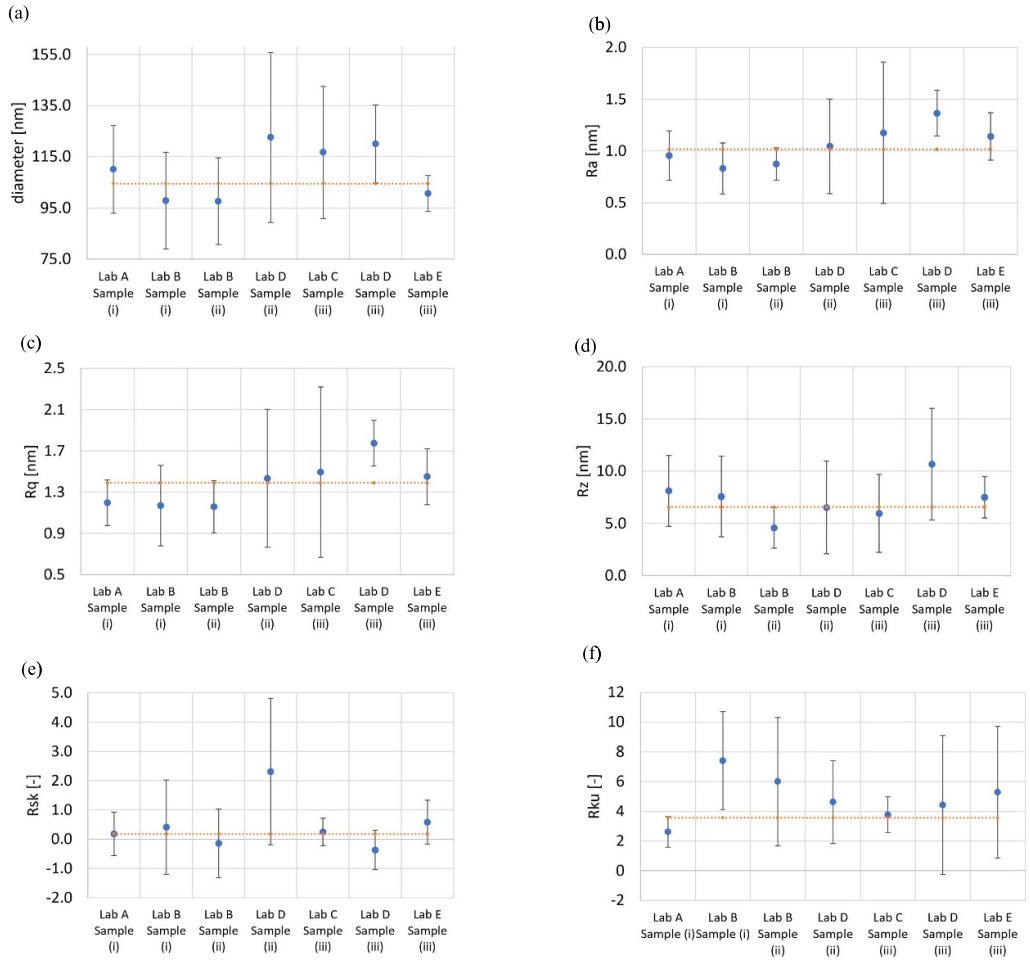


**Figure 10.** Results of the various participants on three different samples regarding roughness evaluation, in particular (a) NWs diameter measured as top-height of the circle base, (b) average roughness *Ra*, (c) root mean square roughness *Rq*, (d) maximum roughness height *Rz*, (e) roughness skewness *R*sk, and (f) roughness kurtosis *R*ku. Please note that error bars refer to standard deviation of the weighted mean values, represented by the orange line.

the value evaluated by TEM (figure 1(k)), *i.e.* 107 nm. Figure 10(b)–(f) report mean weighted mean values together with the standard deviation, that represents the dispersion between the different NWs deposited onto the surface. Please note that different software packages were used in the analysis of these results, including MountainsLab, a MATLAB (MathWorks) routine and a Python routine. The goal of our study is to compare the results, independently on the type of software or routine used. The uncertainties due to the different types of software are considered into the repeatability and reproducibility term in the uncertainty budgets.

More in general, this paper is not about a study to investigate what method is preferred for measuring these specific parameters. Various measurement methods and analysis tools were used on purpose in order to try to get consistent measurement results despite a variety of instruments, methods and analysis tools.

Observing particularly Lab C, it could be noted that the error bars are larger than the other labs. It could be explained by the fact that Lab C measured a larger number of NWs (12 instead of around 5 for the other labs), highlighting the NW size distribution is not negligible in the measurement of topographic information of NWs.

The plots show a good consistency of results, as can be appreciated by the overlap of the standard deviation bars. The experimental data from the various laboratories present a standard deviation of about 20% compared to *Ra*, *Rq* and *R*ku weighted mean values, while the standard deviation is greater than 50% for *R*sk and *Rz* weighted mean values. Regarding top-height diameter *d* measurements, the standard deviation is the 15% of the mean value. The standard deviations here represent the reproducibility between the different laboratories. This reproducibility includes components linked to data acquisition (differences between instruments and method) and data analysis (operator, software packages).

### *6.2. Roughness comparison on same set of NWs measured by different laboratories*

In order to explain the difference observed by each participant in roughness and height measurements, exactly the same data treatment by the same operator was applied on the same set of NWs.

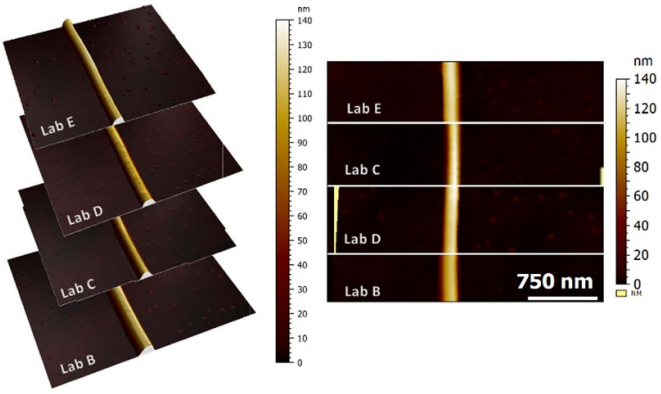


**Figure 11.** Colocalized AFM images of the same nanowire acquired by four different laboratories.

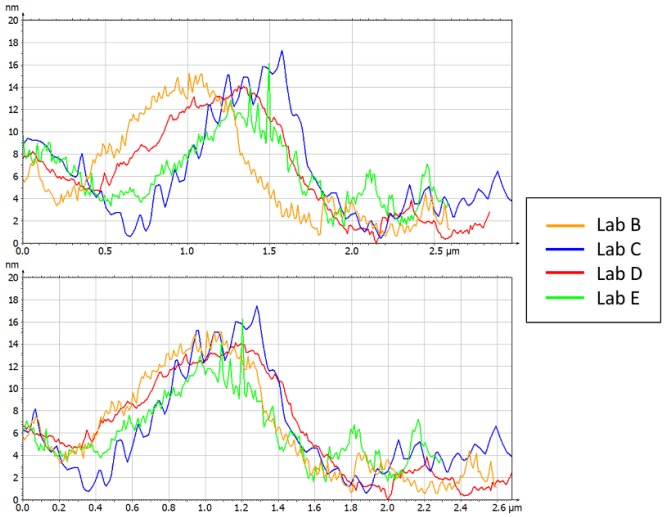


**Figure 12.** Top-height profile on exactly the same nanowire of figure 11. (Top) without distortion corrections (bottom) with distortion correction.

First, each image (calibrated and levelled) of the nanowire to be compared was colocalized to extract exactly the same area on the nanowire, without contamination (figure 11) with Mountains Lab software (v10, Digital Surf). The pixel size of each colocalized image is different in function of the laboratory which makes the measurement. This colocalization process make the set of images acquired at the same location to be overlay. This co-location step involves distorting the overlay images relative to the image that has been imposed as a reference.

Then, a MATLAB (MathWorks) routine is used to extract the top-height profile for the colocalized images (figure 12), and the same trend is found for the various top-height profiles along *Y* axis extracted from the various images (figure 11) analyzed by the different AFMs.

Some distortions along the NW direction are due to drift in XY direction during the image acquisition not properly corrected by the colocalization process. A correction is performed directly on profiles (figure 12).

Finally, the roughness parameters are extracted from the profiles, using a Gaussian *L*-filter before calculation, by means of MountainsSPIP (DigitalSurf) software.

The results are presented in table 1. Some differences are probably due to (i) the evaluation was performed on portions of images with different pixel size sampling, and (ii) the lateral distortions of the co-localized images.

## 7. Uncertainty estimation

### 7.1. Diameter

In the appendix the uncertainty budget of each partner according to the GUM—Guide to the expression of Uncertainty in Measurement [48] is reported. Hereafter, in In table 2 a summary table of the expanded uncertainties is reported.

For each uncertainty source, together with the estimate and its standard uncertainty, is also reported the uncertainty type, which can be experimentally evaluated through a statistical analysis on a series of observations (*A*-type), or based on previous measures, certificate values or on theoretical assumptions of statistics that characterize a measurement process (*B*-type).

The probability density function (PDF), which is the mathematical function describing the probability that the value

**Table 1.** Roughness results of the profiles reported in figure 12.

| | *Ra* (nm) | *Rq* (nm) | *Rz* (nm) | *Rsk* | *Rku* |
|---|---|---|---|---|---|
| *Mean* | 0.7 | 0.9 | 2.1 | 0.4 | 5.8 |
| *Standard deviation* | 0.2 | 0.2 | 0.7 | 0.3 | 4.4 |

**Table 2.** Expanded uncertainty values of the NW diameter for each Lab. A more deep focus for each Lab can be found in the appendix.

| Laboratory | Expanded uncertainty of the NW diameter ($k$ =2) $U$ (nm) |
|---|---|
| Lab A | 5.0 |
| Lab B | 6.2 |
| Lab C | 7.1 |
| Lab D | 5.4 |
| Lab E | 6.8 |

of the variable lies within that interval, which can be normal (indicated with $N$), when the source of uncertainty has a Gaussian distribution, or rectangular (indicated with $R$), if the source of uncertainty has the same probability of being contained within an interval.

$\nu_i$ indicates the degrees of freedom, which give information about the reliability of the uncertainty value, while $\nu_{\text{eff}}$ is the effective degrees of freedom of the combined standard uncertainty calculated using the Welch-Satterthwaite formula. In all budgets reported in appendix, the degrees of freedom for $A$-type uncertainty depend on the observations, while for the $B$-type is set equal to 100 if is available in calibration certificates or equal to 50 if it derives from previous knowledge or published reports.

The sensitivity coefficient describes the extent to which the source of uncertainty influences the overall uncertainty. The uncertainty contribution to the estimated quantity gives the final contribution from a given source of uncertainty to the overall uncertainty.

The combined standard uncertainty is the overall uncertainty of the estimated quantity calculated by combining the individual values according to the law of propagation of uncertainty. The expanded uncertainty is obtained by multiplying the combined standard uncertainty with the coverage factor $k = 2$, in order to have the 95% level of confidence to be associated with the interval.

Please notice that the equation used for each uncertainty budget evaluation is equal to $d = C \cdot d_{\text{mean}} + \delta_{\text{noise}}$, where $d$ is the top-height diameter obtained as explained in section 5 and $d_{\text{mean}}$ is the average of the diameter form experimental data, $C$ is the calibration of the instrument, and $\delta_{\text{noise}}$ is the instrumental noise. In these budgets, the influence of the temperature and the tip-sample-substrate interactions are not considered since they are negligible terms.

Each participant differs slightly in the evaluation according to the knowledge of the system, and in appendix, tables 1–5 all contributions are described.

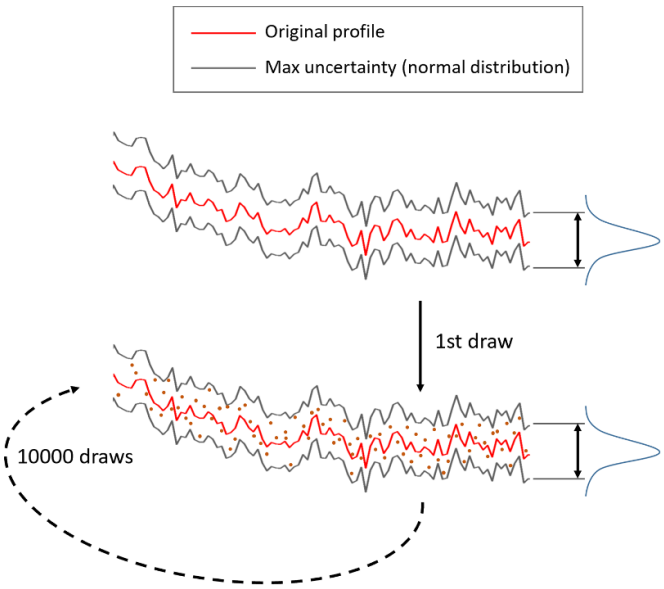


**Figure 13.** Schema and explaining the Monte Carlo method developed for the evaluation of the uncertainty of nanowires roughness.

The combined standard uncertainty regarding top-height diameter is 2.0% for Lab A, 2.8% for Lab D and Lab E, and 2.9% for Lab B and Lab C.

### 7.2. Roughness parameters

Uncertainty calculation of roughness parameters is a very important task, due to the growing importance of roughness in applications at the nanoscale [49].

Since the standard ISO 19606:2017 [50] describes the evaluation with AFM of few roughness parameters but does not deal with the uncertainty, we decided to evaluate the uncertainty for each roughness measurands by using a Monte Carlo approach (figures 13 and 14(a)), as recommended by the Guide to the expression of Uncertainty in Measurement [51].

At first, our approach consists in generating 10 000 profiles according to the following formula:

$$P_i = P_0 + u_r \cdot P_0 \cdot \boldsymbol{N}_1 + \delta_{\text{noise}} \cdot \boldsymbol{N}_2$$

where $P_i$ is the profile generate at the $i$th iteration, $P_0$ is the original profile, $u_r$ is the relative uncertainty of the $Z$-calibration coefficient (based on the relative standard uncertainty of the

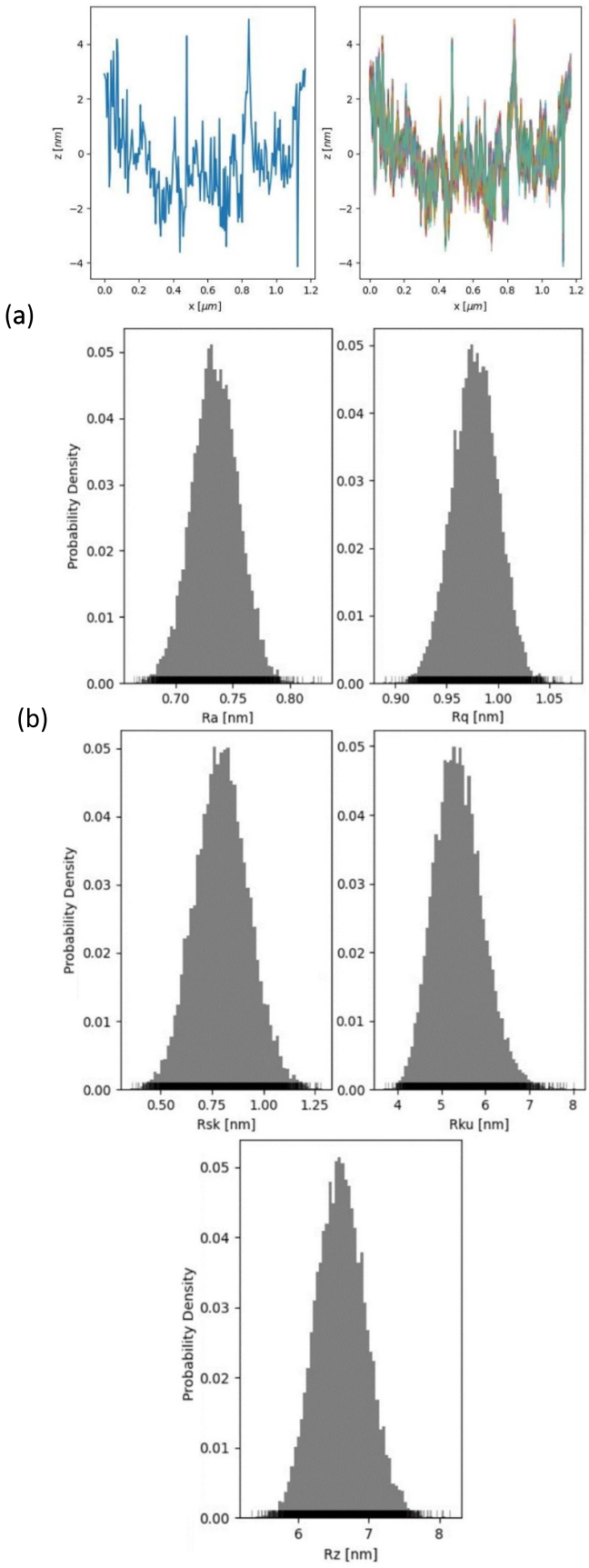


**Figure 14.** (a) Roughness profile along nanowire length (left) and random profiles generated by Monte Carlo simulation (right). (b) Probability density function of roughness parameters by Monte Carlo evaluation.

**Table 3.** Uncertainty results for roughness parameters according to Monte Carlo evaluation.

| Roughness parameter | Laboratory | Expanded uncertainty ($k = 2$) $U$ (nm) |
|---|---|---|
| *Ra* | Lab A | 0.01 |
| | Lab B | 0.09 |
| | Lab C | 0.05 |
| | Lab D | 0.01 |
| | Lab E | 0.03 |
| *Rq* | Lab A | 0.01 |
| | Lab B | 0.10 |
| | Lab C | 0.07 |
| | Lab D | 0.01 |
| | Lab E | 0.04 |
| *Rz* | Lab A | 0.22 |
| | Lab B | 1.98 |
| | Lab C | 1.00 |
| | Lab D | 0.35 |
| | Lab E | 1.18 |
| *Rsk* | Lab A | 0.07 |
| | Lab B | 0.82 |
| | Lab C | 0.39 |
| | Lab D | 0.22 |
| | Lab E | 0.48 |
| *Rku* | Lab A | 0.33 |
| | Lab B | 5.27 |
| | Lab C | 1.66 |
| | Lab D | 1.13 |
| | Lab E | 3.23 |

used step height standard), $\delta_{\text{noise}}$ is the $Z$-noise of the instrument (noise measurement on a very flat and smooth surface), and $\boldsymbol{N}_1, \boldsymbol{N}_2 \in \mathbb{R}^{n_p}$ are random vectors of size $n_p$ (number of pixel in the profile) extracted from a normal distribution.

Afterwards, for each iteration we evaluate roughness parameters, and then parse the obtained distributions until 95% coverage is reached, so these represent the expanded uncertainty for each roughness parameter (figure 14(b)).

Please note that two different software packages were used, a MATLAB routine and a Python routine.

The results are presented for scans at different locations to indicate the consistency of the measurements. The average values, and the corresponding combined and expanded uncertainties, were calculated from sets of results of different sizes, as reported in table 3. The combined standard uncertainty results for the various laboratories range from 0.3% to 5.0% for *Ra* values, from 0.3% to 4.4% for *Rq* values, from 1.4% to 8.4% for *Rz* values, from 4.8% to 20.1% for *R*sk values, and from 6.3% to 18.0% for *R*ku values.

The big advantage of using this Monte Carlo approach is that it automatically deals with the error propagation for non-analytical measurement functions and correctly handles correlations between uncertainty sources.

## 8. Conclusions

This study reports an interlaboratory comparison on the measurements of dimensional parameters of NWs by AFMs among some European national metrology institutes. The studied descriptors are height and roughness of metal-assisted chemically etched NWs. In fact, both are key parameters to understand if the fabrication process was carried out in a correct way. Moreover, the exact knowledge of these parameters is essential to achieve the expected functional characteristic of energy harvesting systems based on NWs.

Since methods to measure NWs is lacking, and prevents studies from being comparable, particularly with regard to roughness, in this work we develop a method to measure and compare height and roughness of exactly the same set of NWs.

Concerning the height, many comparisons had already been realized for nanoparticle sizing, but not for NWs. Experimental data shows a good consistency, and the standard deviation is the 15% of the top-height diameter mean value. Moreover, combined standard uncertainties given are included in a range from 2.2% to 2.9%.

Concerning the roughness, even on flat surfaces, very few comparisons are existing for the calculation of these parameters with AFM. No standard or guide exists for assessing the uncertainty associated with it. We propose in this work a methodology, based on Monte-Carlo approach to evaluate it. This strategy was implemented by two teams involved in this study into two different programming languages. The results are consistent (combined standard uncertainty results ranging from 0.3% to 5.0% for *Ra* values, and from 0.3% to 4.4% for *Rq* values), proving that this methodology is particularly adapted to this study.

Finally, it must be noted that in this work, several different metrological software and routines based on MATLAB and Python environments were used and consistently compared.

## Data availability statement

The data that support the findings of this study are openly available at the following URL/DOI: https://doi.org/10.5281/zenodo.10887767.

## Acknowledgments

This research project is supported by the European Union and is funded within the scope of the European Metrology Programme for Innovation and Research (EMPIR) project 19ENG05 NanoWires entitled ‘High throughput metrology for nanowire energy harvesting devices’ (www.ptb.de/empir2020/20nanowires/home/).

Part of this work has received funding from the European Union’s Horizon 2020 research and innovation programme under grant agreement No 101007417, having benefited from the access provided by CEA LETI in Grenoble within the framework of the NFFA-Europe Pilot Transnational Access Activity, proposal [ID310].

Part of this work has been carried out at Nanofacility Piemonte, a laboratory supported by the ‘Compagnia di San Paolo’ Foundation, and at QR Lab—Micro&Nanolaboratories, INRiM.

The authors also desire to Acknowledge the Italian Piedmont Region project ‘Piemonte Quantum Enabling Technologies’ (PiQuET) within the ‘Infra-P’ scheme (POR-FESR 2014−2020 program of the European Union).

## Appendix

**Appendix Table 1.** Uncertainty budget evaluation for the top-height diameter for Lab A measurements.

| Source of uncertainty | Quantity | Unit | Estimate | Standard uncertainty of estimate | Uncertainty type | PDF | $\nu_i$ | Sensitivity coefficients | Standard uncertainty of measurand |
|---|---|---|---|---|---|---|---|---|---|
| *Repeatability* | $d_{\text{mean}}$ | nm | 110.1 | 2.2 | A | N | 10 | $C$ | 2.2 |
| *instrument calibration* | $C$ | — | 1.0 | 0.1 | A | N | 50 | $d_{\text{mean}}$ | 0.1 |
| *Noise* | $\delta_{\text{noise}}$ | nm | 0.0 | 0.1 | A | R | 50 | 1 | 0.1 |
| | | | | | | | | | Total value |
| Combined standard uncertainty | | | | | | | | $u$ (nm) | **2.2** |
| Effective degrees of freedom $\nu_{\text{eff}}$—Welch-Satterthwaite formula | | | | | | | | | 10 |
| Coverage factor | | | | | | | | | 2.28 |
| Expanded uncertainty ($k$ =2) | | | | | | | | $U$ (nm) | **5.0** |

The repeatability considers the standard deviation of the mean of the NWs analyzed, which were 5 as reported in the degrees of freedom.
The $C$ factor considers (i) the calibration, that takes into account the interferometric calibration of the $Z$ axis including cosine errors, (ii) the piezoelectric non-linearity, and (iii) the resolution of the digital-to-analog converter on the piezoelectric stroke of 2 μm.
The profile noise was evaluated from several measurements on portions of images with the silicon substrate only.

**Appendix Table 2.** Uncertainty budget evaluation for the top-height diameter for Lab B measurements.

| Source of uncertainty | Quantity | Unit | Estimate | Standard uncertainty of estimate | Uncertainty type | PDF | $\nu_i$ | Sensitivity coefficients | Standard uncertainty of measurand |
|---|---|---|---|---|---|---|---|---|---|
| *Repeatability* | $d_{\text{mean}}$ | nm | 97.6 | 2.5 | A | N | 10 | $C$ | 2.6 |
| *Instrument calibration* | $C$ | — | 1.0 | 1.1 | A | N | 15 | $d_{\text{mean}}$ | 1.1 |
| *Noise* | $\delta_{\text{noise}}$ | nm | 0.0 | 0.3 | A | R | 50 | 1 | 0.2 |
| | | | | | | | | | Total value |
| Combined standard uncertainty | | | | | | | | $u$ (nm) | **2.8** |
| Effective degrees of freedom $\nu_{\text{eff}}$—Welch-Satterthwaite formula | | | | | | | | | 13 |
| Coverage factor | | | | | | | | | 2.21 |
| Expanded uncertainty ($k$ =2) | | | | | | | | $U$ (nm) | **6.2** |

The repeatability considers the standard deviation of the mean of the 10 different images analysed.
The standard uncertainty of the calibration of the instrument considers 15 repeated measurements on a step-height standard used to calibrate the $Z$ axis, which was previously characterized by a metrological AFM.
The profile noise was evaluated from several measurements on flat surfaces.

**Appendix Table 3.** Uncertainty budget evaluation for the top-height diameter for Lab C measurements.

| Source of uncertainty | Quantity | Unit | Estimate | Standard uncertainty of estimate | Uncertainty type | PDF | $\nu_i$ | Sensitivity coefficients | Standard uncertainty of measurand |
|---|---|---|---|---|---|---|---|---|---|
| *Repeatability* | $d_{\text{mean}}$ | nm | 116.7 | 3.3 | A | N | 10 | $C$ | 3.3 |
| *Instrument calibration* | $C$ | — | 1.0 | 0.6 | A | N | 130 | $d_{\text{mean}}$ | 0.6 |
| *Noise* | $\delta_{\text{noise}}$ | nm | 0.0 | 0.2 | B | N | 50 | 1 | 0.2 |
| | | | | | | | | | Total value |
| Combined standard uncertainty | | | | | | | | $u$ (nm) | **3.4** |
| Effective degrees of freedom $\nu_{\text{eff}}$—Welch-Satterthwaite formula | | | | | | | | | 21 |
| Coverage factor | | | | | | | | | 2.13 |
| Expanded uncertainty ($k$ =2) | | | | | | | | $U$ (nm) | **7.1** |

The repeatability term considers the variation on height on different portions of the same wire.
The $C$ term considers the (i) calibration of the step-height standard, (ii) the instrument repeatability along $Z$ axis, (iii) the sensor resolution limit, and (iv) the scan speed influence.
The profile noise was evaluated from previous measurements on mica surfaces.

**Appendix Table 4.** Uncertainty budget evaluation for the top-height diameter for Lab D measurements.

| Source of uncertainty | Quantity | Unit | Estimate | Standard uncertainty of estimate | Uncertainty type | PDF | $\nu_i$ | Sensitivity coefficients | Standard uncertainty of measurand |
|---|---|---|---|---|---|---|---|---|---|
| *Reproducibility* | $d_{\text{mean}}$ | nm | 158.8 | 2.4 | A | N | 100 | $C$ | 2.4 |
| *Instrument calibration* | $C$ | — | 1.0 | $7{\cdot}10^{-3}$ | A | N | 260k | $d_{\text{mean}}$ | 1.1 |
| *Noise* | $\delta_{\text{noise}}$ | nm | 0.0 | 0.1 | A | N | 1000k | 1 | 0.1 |
| | | | | | | | | | Total value |
| Combined standard uncertainty | | | | | | | | $u$ (nm) | **2.7** |
| Effective degrees of freedom $\nu_{\text{eff}}$—Welch-Satterthwaite formula | | | | | | | | | 150 |
| Coverage factor | | | | | | | | | 2 |
| Expanded uncertainty ($k$ =2) | | | | | | | | $U$ (nm) | **5.4** |

The uncertainty term due to the reproducibility is studied by considering, as the most representative, the experimental value results with the highest reproducibility. The 100 DOF is the estimate of the number of lines used to calculate the average height.
The relative standard uncertainty of the $C$ factor arises from the calibration of the $Z$-range with the physical step height standards, and it is equal to the relative standard measurement uncertainty of the calibration process with the interference microscope that was used to calibrate the step height standards. Please note that the standard uncertainty of the instrument calibration factor is calculated by multiplying the relative standard uncertainty and the measured height.
The profile noise was evaluated as on 'stationary measurements', where it was set a scan range of 0 nm × 0 nm and was recorded a time signal only.

**Appendix Table 5.** Uncertainty budget evaluation for the top-height diameter for Lab E measurements.

| Source of uncertainty | Quantity | Unit | Estimate | Standard uncertainty of estimate | Uncertainty type | PDF | $\nu_i$ | Sensitivity coefficients | Standard uncertainty of measurand |
|---|---|---|---|---|---|---|---|---|---|
| *Repeatability* | $d_{\text{mean}}$ | nm | 100.7 | 2.7 | A | N | 10 | $C$ | 2.6 |
| *Instrument calibration* | $C$ | — | 0.9 | 1.1 | A | N | 15 | $d_{\text{mean}}$ | 1.1 |
| *Noise* | $\delta_{\text{noise}}$ | nm | 0.0 | 0.2 | A | R | 50 | 1 | 0.1 |
| | | | | | | | | | Total value |
| Combined standard uncertainty | | | | | | | | $u$ (nm) | **2.8** |
| Effective degrees of freedom $\nu_{\text{eff}}$—Welch-Satterthwaite formula | | | | | | | | | 6.9 |
| Coverage factor | | | | | | | | | 2.43 |
| Expanded uncertainty ($k$ =2) | | | | | | | | $U$ (nm) | **6.8** |

The uncertainty was evaluated in the same way as done for Lab B.
It should be noted that these uncertainty budgets do not consider the interactions between the substrate and the nanowire. Two main reasons explain that choice: the first is that one related to the evaluation of the elastic moduli of both nanowires and AFM tip, which are similar and both hard materials. Moreover, as the microscopist cannot be sure that the NW is touching the substrate well, a careful selection of NW has been realized before measurement. Although identified, these sources cannot be estimated.

## ORCID iDs

Luigi Ribotta https://orcid.org/0000-0001-5334-5246
Alexandra Delvallée https://orcid.org/0000-0002-8908-0742
Eleonora Cara https://orcid.org/0000-0002-5981-9569
Andrea Giura https://orcid.org/0009-0000-2761-641X
Ivan De Carlo https://orcid.org/0000-0002-4066-8107
Luca Boarino https://orcid.org/0000-0002-1221-2591

## References

[1] Kirsch S 2020 Running out? Rethinking resource depletion *Extrem. Ind. Soc.* **7** 838–40
[2] Perera F 2017 Pollution from fossil-fuel combustion is the leading environmental threat to global pediatric health and equity: solutions exist *Int. J. Environ. Res. Public Health* **15** 16
[3] Ucal M and Xydis G 2020 Multidirectional relationship between energy resources, climate changes and sustainable development: technoeconomic analysis *Sustain. Cities Soc.* **60** 102210
[4] Global Industry Research2024 Energy harvesting market size and growth insights, leading players updates by 2031 (available at: www.linkedin.com/pulse/energy-harvesting-market-size-growth-insights-dzvyf/) (Accessed 22 February 2024)
[5] International Energy Agency, International Energy Agency (IEA) Web Page (available at: www.iea.org/energy-system/renewables/solar-pv) (Accessed 22 February 2024)
[6] Ko S H 2014 Review of the multi-scale nano-structure approach to the development of high efficiency solar cells *Smart Sci.* **2** 54–62
[7] Kraemer D *et al* 2011 High-performance flat-panel solar thermoelectric generators with high thermal concentration *Nat. Mater.* **10** 532–8
[8] Zhao X, Wei C M, Yang L and Chou M Y 2004 Quantum confinement and electronic properties of silicon nanowires *Phys. Rev. Lett.* **92** 236805

[9] Irrera A, Artoni P, Iacona F, Pecora E F, Franzò G, Galli M, Fazio B, Boninelli S and Priolo F 2012 Quantum confinement and electroluminescence in ultrathin silicon nanowires fabricated by a maskless etching technique *Nanotechnology* **23** 075204

[10] Hochbaum A I, Chen R, Delgado R D, Liang W, Garnett E C, Najarian M, Majumdar A and Yang P 2008 Enhanced thermoelectric performance of rough silicon nanowires *Nature* **451** 163–7

[11] Ferrando-Villalba P *et al* 2018 Impact of pore anisotropy on the thermal conductivity of porous Si nanowires *Sci. Rep.* **8** 12796

[12] Antidormi A *et al* 2018 Physical and chemical control of interface stability in porous Si–eumelanin hybrids *J. Phys. Chem.* C **122** 28405–15

[13] Graniel O *et al* 2018 Optical properties of ZnO deposited by atomic layer deposition (ALD) on Si nanowires *Mater. Sci. Eng.* **236–237** 139–46

[14] Brand Uwe 19ENG05 NanoWires Project EMPIR programme webpage (available at: www.ptb.de/empir2020/nanowires/project/overview/) (Accessed 08 November 2023)

[15] Hussain D, Ahmad K, Song J and Xie H 2017 Advances in the atomic force microscopy for critical dimension metrology *Meas. Sci. Technol.* **28** 012001

[16] Thiesler J, Ahbe T, Tutsch R and Dai G 2022 True 3D nanometrology: 3D-Probing with a cantilever-based sensor *Sensors* **22** 314

[17] Hong W K, Song S, Hwang D-K, Kwon S-S, Jo G, Park S-J and Lee T 2008 Effects of surface roughness on the electrical characteristics of ZnO nanowire field effect transistors *Appl. Surf. Sci.* **254** 7559–64

[18] Seoane N, Martinez A, Brown A R and Asenov A 2009 Study of surface roughness in extremely small Si nanowire MOSFETs using fully-3D NEGFs *Proc. 2009 Spanish Conf. Electron Devices, CDE'09* pp 180–3

[19] Hosseinzadeh Khaligh H and Goldthorpe I A 2014 Hot-rolling nanowire transparent electrodes for surface roughness minimization *Nanoscale Res. Lett.* **9** 1–5

[20] Li Z, Leung C, Gao F and Gu Z 2015 Effects of nanowire length and surface roughness on the electrochemical sensor properties of nafion-free, Vertically aligned pt nanowire array electrodes *Sensors* **15** 22473–89

[21] Lim J, Hippalgaonkar K, Andrews S C, Majumdar A and Yang P 2012 Quantifying surface roughness effects on phonon transport in silicon nanowires *Nano Lett.* **12** 2475–82

[22] Svizhenko A, Leu P W and Cho K 2007 Effect of growth orientation and surface roughness on electron transport in silicon nanowires *Phys. Rev.* B **75** 125417

[23] McSweeney W, Glynn C, Geaney H, Collins G, Holmes J D and O'Dwyer C 2015 Mesoporosity in doped silicon nanowires from metal assisted chemical etching monitored by phonon scattering *Semicond. Sci. Technol.* **31** 014003

[24] Kim H, Park Y-H, Kim I, Kim J, Choi H-J and Kim W 2011 Effect of surface roughness on thermal conductivity of VLS-grown rough $Si_{1-x}Ge_x$ nanowires *Appl. Phys.* A **104** 23–28

[25] Stranz A, Waag A and Peiner E 2013 High-temperature performance of stacked silicon nanowires for thermoelectric power generation *J. Electron. Mater.* **42** 2233–8

[26] Murataj I *et al* 2023 Hybrid metrology for nanostructured optical metasurfaces *ACS Appl. Mater. Interfaces* **15** 57992–8002

[27] Siaudinyte L, Hansen P E, Koops R, Xu J and Peiner E 2023 Hybrid metrology for nanometric energy harvesting devices *Meas. Sci. Technol.* **34** 094008

[28] Crouzier L, Delvallée A, Ducourtieux S, Devoille L, Noircler G, Ulysse C, Taché O, Barruet E, Tromas C and Feltin N 2019 Development of a new hybrid approach combining AFM and SEM for the nanoparticle dimensional metrology *Beilstein J. Nanotechnol.* **10** 1523–36

[29] Feltin N *et al* 2023 Metrological protocols for reaching reliable and SI-traceable size results for multi-modal and complexly shaped reference nanoparticles *Nanomaterials* **13** 993

[30] Huang Z, Geyer N, Werner P, de Boor J and Gösele U 2011 Metal-assisted chemical etching of silicon: a review *Adv. Mater.* **23** 285–308

[31] Cara E, Mandrile L, Ferrarese Lupi F, Giovannozzi A M, Dialameh M, Portesi C, Sparnacci K, De Leo N, Rossi A M and Boarino L 2018 Influence of the long-range ordering of gold-coated Si nanowires on SERS *Sci. Rep.* **8** 11305

[32] Li X and Bohn P W 2000 Metal-assisted chemical etching in $HF/H_2O_2$ produces porous silicon *Appl. Phys. Lett.* **77** 2572–4

[33] Maurino V, Pellegrino F, Picotto G B and Ribotta L 2022 Quantitative three-dimensional characterization of critical sizes of non-spherical $TiO_2$ nanoparticles by using atomic force microscopy *Ultramicroscopy* **234** 113480

[34] Consultative Committee for Length, CIPM 2019 Mise en pratique for the definition of the metre in the SI *SI Brochure 9th* Append. 2 edn (available at: https://www.bipm.org/en/publications/mises-en-pratique)

[35] ISO 14644-1:2015(en) 2015 Cleanrooms and associated controlled environments—Part 1: classification of air cleanliness by particle concentration

[36] Delvallée A, Feltin N, Ducourtieux S, Trabelsi M and Hochepied J F 2015 Toward an uncertainty budget for measuring nanoparticles by AFM *Metrologia* **53** R1–R11

[37] Ducourtieux S and Poyet B 2011 Development of a metrological atomic force microscope with minimized Abbe error and differential interferometer-based real-time position control *Meas. Sci. Technol.* **22** 094010

[38] Koops R, van Veghel M and van de Nes A 2016 A virtual lateral standard for AFM calibration *Microelectron. Eng.* **153** 29–36

[39] Picotto G B, Vallino M and Ribotta L 2020 Tip–sample characterization in the AFM study of a rod-shaped nanostructure *Meas. Sci. Technol.* **31** 084001

[40] Meli F *et al* 2012 Traceable size determination of nanoparticles, a comparison among European metrology institutes *Meas. Sci. Technol.* **23** 125005

[41] ASTM E2859-11 2017 *Standard Guide for Size Measurement of Nanoparticles Using Atomic Force Microscopy* (https://doi.org/10.1520/E2859-11)

[42] Boyd R *et al* 2011 Good Practice Guide No. 119 good practice guide for the determination of the size and size distribution of spherical nanoparticle samples p 80

[43] Vobornik D, Chen M, Zou S and Lopinski G P 2023 Measuring the diameter of single-wall carbon nanotubes using AFM *Nanomaterials* **13** 477

[44] ISO 21920:2021 2021 Geometrical product specifications (GPS) Surface texture: profile part 1: indication of surface texture (available at: www.iso.org/standard/72196.html)

[45] Ribotta L 2022 Dimensional metrology at the nanoscale: quantitative characterization of nanoparticles by means of metrological atomic force microscopy *PhD Thesis* Politecnico di Torino

[46] Garnaes J 2011 Diameter measurements of polystyrene particles with atomic force microscopy *Meas. Sci. Technol.* **22** 094001

[47] Marinello F, Balcon M, Schiavuta P, Carmignato S and Savio E 2011 Thermal drift study on different commercial scanning probe microscopes during the initial warming-up phase *Meas. Sci. Technol.* **22** 094016

[48] Joint Committee for guides in Metrology 2008 Evaluation of measurement data—guide to the expression of uncertainty

in measurement *Int. Organ. Stand. Geneva ISBN* vol 50 p 134

[49] Marinello F, La Storia A, Mauriello G and Passeri D 2019 Atomic force microscopy techniques to investigate activated food packaging materials *Trends Food Sci. Technol.* **87** 84–93

[50] ISO 19606:2017 2017 *Fine ceramics (advanced ceramics, advanced technical ceramics)—test method for surface roughness of fine ceramic films by atomic force microscopy* (available at: www.iso.org/standard/65457.html)

[51] Joint Committee for guides in Metrology 101:2008 2008 Evaluation of measurement data—Supplement 1 to the "Guide to the expression of uncertainty in measurement" *Propagation of distributions using a Monte Carlo method Évaluation*